I. THERMODYNAMIC BEHAVIOR NEAR THE NEMATIC AND MAGNETIC PHASE TRANSITIONS - THEORY

We follow Ref. [36] of the main text to compute the thermodynamic properties near the nematic and magnetic phase transitions for an anisotropic three-dimensional system. The partition function can be formulated as a path integral $Z \equiv \mathrm{Tr}\left\{\exp(-\beta H)\right\} = \int \mathcal{D}\left[\mathbf{m}_1, \mathbf{m}_2\right] \exp\left(-W\left[\mathbf{m}_1, \mathbf{m}_2\right]\right)$, where the effective action is given by:

$$W\left[\mathbf{m}_1, \mathbf{m}_2\right] = \frac{1}{2}\sum_{\mathbf{q}} \chi_{0,\mathbf{q}}^{-1}\left(|\mathbf{m}_{1\mathbf{q}}|^2 + |\mathbf{m}_{2\mathbf{q}}|^2\right) + \frac{1}{4N}\int_{\mathbf{r}}\left[u\left(\mathbf{m}_1^2 + \mathbf{m}_2^2\right)^2 - g\left(\mathbf{m}_1^2 - \mathbf{m}_2^2\right)^2\right]$$

Here the bare magnetic susceptibility is given by $\chi_{0,\mathbf{q}}^{-1} = r_0\left(T\right) + f_{\mathbf{q}}$, where the bare mass r_0 is a monotonic function of temperature. We take $f_{\mathbf{q}} = q_x^2 + q_y^2 + 4\zeta \sin^2\frac{q_z}{2}$ to account for anisotropic magnetic fluctuations along the z-axis. $\mathbf{q}$ measures the small deviation from the ordering wavevector $\mathbf{Q}_{i=1,2}$. $\sum_{\mathbf{q}}$ is short for $V\int \frac{\mathrm{d}^d q}{(2\pi)^d}$. N denotes the number of vector components of $\mathbf{m}_{i=1,2}$. Physically N = 3 if full spin SU(2) symmetry is present. $\{u, g\}$ are quartic coupling constants. $u > g > 0$ is required for the stability of the effective action against large-amplitude fluctuations. Here since we are considering thermal phase transitions, we omit the correlations along imaginary time axis, and absorb temperature into the dimensionless parameters of the model, namely $\{r_0, \zeta, u, g\}$.

The free energy is related to the action by $F = -T\ln Z$. The entropy (S) and heat capacity (C) are calculated from first and second derivatives of the free energy with respect to temperature, i.e., $S = -\partial F/\partial T$ and $C = T\partial S/\partial T$.

To incorporate the impact of fluctuations, we decouple the quartic interactions using two Hubbard-Stratonovich fields $\{\psi, \phi\}$, to obtain:

$$Z = \int \mathcal{D}\left[\mathbf{m}_1, \mathbf{m}_2, \psi, \phi\right] e^{-W_{\mathrm{eff}}}$$

where

$$W_{\mathrm{eff}} = -\frac{N\psi^2}{u} + \frac{N\phi^2}{g} + \frac{1}{2}\sum_{\mathbf{q}}\left[\left(\chi_{0,\mathbf{q}}^{-1} + \psi - \phi\right)|\mathbf{m}_{1\mathbf{q}}|^2 + \left(\chi_{0,\mathbf{q}}^{-1} + \psi + \phi\right)|\mathbf{m}_{2\mathbf{q}}|^2\right]$$

Integrating out magnetic fluctuations, we obtain:

$$W_{\mathrm{eff}}\left[r, \phi\right] = N\left\{-\frac{\left(r - r_0\right)^2}{u} + \frac{\phi^2}{g} + \frac{1}{2}\sum_{\mathbf{q}}\ln\left[\left(r + f_{\mathbf{q}}\right)^2 - \phi^2\right] + \frac{1}{4\pi}\left(r - \phi\right)\mathrm{M}^2\right\}$$

Here we have accounted for the magnetically ordered state, when $\langle\mathbf{m}_{1\mathrm{q}}\rangle = \sqrt{\frac{N}{2\pi}}\mathbf{M} \neq 0$. In the large-N limit, the action can be solved within the saddle-point approximation, obtained from:

$$\begin{aligned} r &= r_0 + \frac{u}{2}\sum_{\mathbf{q}}\frac{r + f_{\mathbf{q}}}{\left(r + f_{\mathbf{q}}\right)^2 - \phi^2} + \frac{u}{8\pi}\mathrm{M}^2 \\ \phi &= \frac{g}{2}\sum_{\mathbf{q}}\frac{\phi}{\left(r + f_{\mathbf{q}}\right)^2 - \phi^2} + \frac{g}{8\pi}\mathrm{M}^2 \\ 0 &= \mathrm{M}\left(r - \phi\right) \end{aligned}$$

Above expressions can be simplified to the following:

$$\begin{aligned} r^* &= r_0^* + \bar{\alpha}\sum_{\kappa=\pm1}\ln\left(\sqrt{r^* + \kappa\phi^* + 4\zeta/\bar{g}} + \sqrt{r^* + \kappa\phi^*}\right) + \bar{\alpha}M^2 \\ \phi^* &= \sum_{\kappa=\pm1}\kappa\ln\left(\sqrt{r^* + \kappa\phi^* + 4\zeta/\bar{g}} + \sqrt{r^* + \kappa\phi^*}\right) + M^2 \\ 0 &= \mathrm{M}\left(r^* - \phi^*\right) \end{aligned}$$

Here we defined

$$\bar{\alpha} \equiv \frac{u}{g};\ \bar{g} \equiv \frac{g}{8\pi};\ \left\{\phi^*, r^*\right\} \equiv \left\{\frac{\phi}{\bar{g}}, \frac{r}{\bar{g}}\right\};\ r_0^* \equiv r_0 - 2\bar{\alpha}\ln\frac{2\Lambda}{\bar{g}}$$

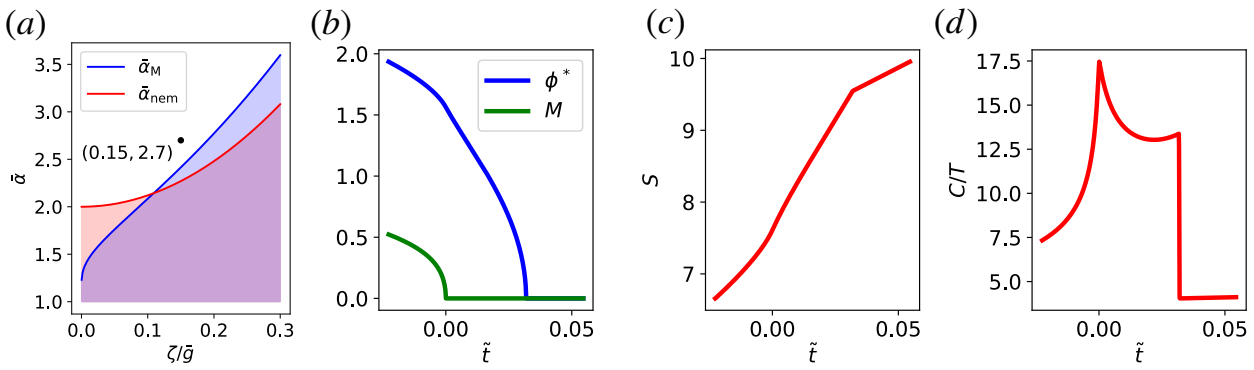

Figure S1. (a) Boundaries in the parameter space of $\{\bar{\alpha}, \zeta/\bar{g}\}$ separating first and second order nematic (red) and magnetic (blue) phase transitions. The shaded areas represent first order transitions. (b-d) The temperature evolution of nematic and magnetic order parameters $\{\phi^*, \mathrm{M}\}$ and the associated contributions to entropy and C/T. The results are obtained using $\bar{\alpha} = 2.7$ and $\zeta/\bar{g} = 0.15$.

where Λ is an upper cutoff to regularize the momentum integration.

We compute the free energy using saddle point solutions:

$$F = -T \ln Z \approx T W_{\text{eff}} [r^*, \phi^*]$$

We define a dimensionless free energy $F^* \equiv \frac{4\pi F}{N\bar{g}T}$. The full analytical expression for $F^*(r_0^*)$ is given by:

$$F^*(r_0^*) = -\frac{(r^* - r_0^*)^2}{2\bar{\alpha}} + \frac{\phi^{*2}}{2} + (r^* - \phi^*) M^2 + \frac{1}{2} \sum_{\kappa=\pm 1} \left[\sqrt{r^* + \kappa\phi^* + 4\zeta/\bar{g}} \sqrt{r^* + \kappa\phi^*} - (2r^* + 2\kappa\phi^* + 4\zeta/\bar{g}) \ln \left(\sqrt{r^* + \kappa\phi^* + 4\zeta/\bar{g}} + \sqrt{r^* + \kappa\phi^*} \right) \right]$$

It is straightforward to show that the saddle point equations can be reproduced by minimizing $F^*(r_0^*)$.

We define a dimensionless variable:

$$\tilde{t} \equiv \frac{r_0^* - r_{0c,N}^*}{r_{0c,N}^*}$$

where $r_{0c,N}^*$ is the location for magnetic phase transition. It is evident that $\tilde{t} \propto t \equiv \frac{T - T_N}{T_N}$, where T_N is the magnetic phase transition temperature measured experimentally.

Therefore, we calculate the entropy and specific heat via $S \propto -\frac{\partial F^*}{\partial \tilde{t}}$ and $C \propto -T \frac{\partial^2 F^*}{\partial \tilde{t}^2}$. The character of the nematic and magnetic phase transitions (continuous or first order, split or simultaneous) depends on two parameters, i.e., the nematic coupling strength $\bar{\alpha}$, and the dimensional anisotropy parameter ζ. In Figure S1(a) we show the magnetic and nematic tricritical lines in the parameter space of $\{\bar{\alpha}, \zeta/\bar{g}\}$. In Figure S1(b-d) we present the temperature evolution of nematic and magnetic order parameters, entropy, and heat capacity coefficient $\frac{C}{T}$ for a certain choice of parameters $\bar{\alpha} = 2.7$ and $\zeta/\bar{g} = 0.15$.

In the inset of Figure 1(b) of the main text, in order to compare theoretically predicted specific heat coefficient $\frac{C}{T}$ to the experimental counterpart, we incorporated a small degree of spatial inhomogeneity. For simplicity, this is done by adding a random mass δr_0^* to the local free energy density. As a result, we compute the averaged free energy by:

$$\bar{F}^*(r_0^*) = \int_{-\infty}^{\infty} \mathrm{d}\delta r_0^* \mathcal{P}(\delta r_0^*) F^*(r_0^* + \delta r_0^*),$$

where we choose a normal distribution function with a small standard deviation ($\sigma = 0.002$). In Figure S2 we plot the disorder averaged results for the same parameters compared to that used in Figure S1(b-d). We see that the dominant effect is on the specific heat behaviors at the nematic and magnetic critical points.

The inset of Figure 1(b) of the main text is obtained by taking the derivative of the disorder averaged C/T with respect to the reduced temperature.

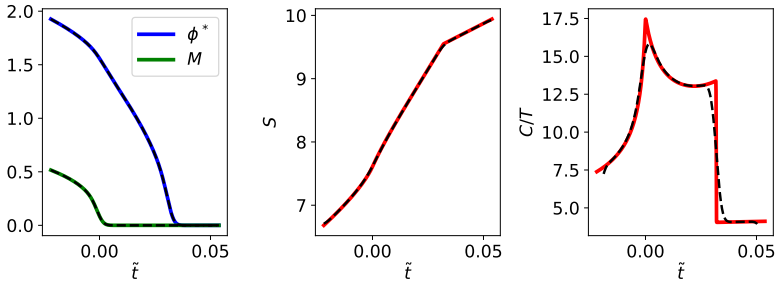

Figure S2. Disorder averaged quantities (dashed lines) for the same parameters used in Figure S1.

II. THERMODYNAMIC BEHAVIOR NEAR THE NEMATIC AND MAGNETIC PHASE TRANSITIONS - EXPERIMENTS

Figure S3 displays the temperature dependence of the volume thermal expansion coefficient (right axis, dashed lines) and the specific heat (left axis, filled squares) of $CeAuSb_2$ at ambient pressure near the nematic and magnetic phase transitions. The volume thermal expansion $\beta = 2\alpha[100] + \alpha[001]$ where $\alpha[100]$ and $\alpha[001]$ are the linear thermal expansion coefficients along [100] and [001], respectively. The arrows indicate the thermal expansion and specific heat jumps used to estimate the pressure dependence of the phase transitions *via* the Ehrenfest relation (Eq. (2) of the main text). The molar volume $V_m \approx 6.0022 \times 10^{-5}$ m^3/mol for $CeAuSb_2$ from x-ray diffraction analysis of the main text. By using the experimental values of $\Delta\beta 1 \approx -14.29 \times 10^{-6}$ K^{-1}, $\Delta\beta 2 \approx 7.05 \times 10^{-6}$ K^{-1}, $\Delta C/T1 \approx 1.1157$ Jmol^{-1}K^{-2}, and $\Delta C/T2 \approx 1.1530$ Jmol^{-1}K^{-2}, we obtain $dT_1/dP \approx -0.77$ K/GPa and $dT_2/dP \approx 0.37$ K/GPa.

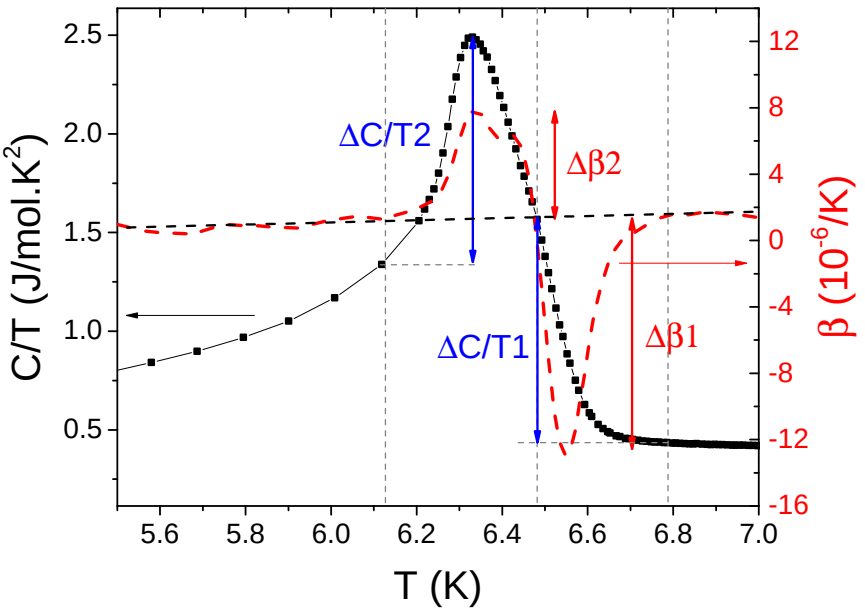

Figure S3. Temperature dependence of the volume thermal expansion coefficient (right axis) and specific heat divided by temperature (left axis) of $CeAuSb_2$ at ambient pressure.

III. MAGNETORESISTANCE OF $CeAuSb_2$

Figure S4 displays the in-plane magnetoresistance of $CeAuSb_2$ at various applied pressures and temperatures below T_N. Solid lines and dashed lines represent upsweeps and downsweeps of magnetic field applied parallel to the c-axis, respectively. At low temperatures, magnetoresistance sharply increases at the first metamagnetic (MM) transition, H_{c1}, and suddenly drops at the second MM transition, H_{c2}, for all pressures. At 1.85 GPa, a new step-like anomaly appears with large hysteresis at H^* between H_{c1} and H_{c2} indicated by red arrows. With increasing temperature, H^* decreases. With increasing pressure, H^* also decreases and finally above 2.16 GPa, H^* is observed below H_{c1}.

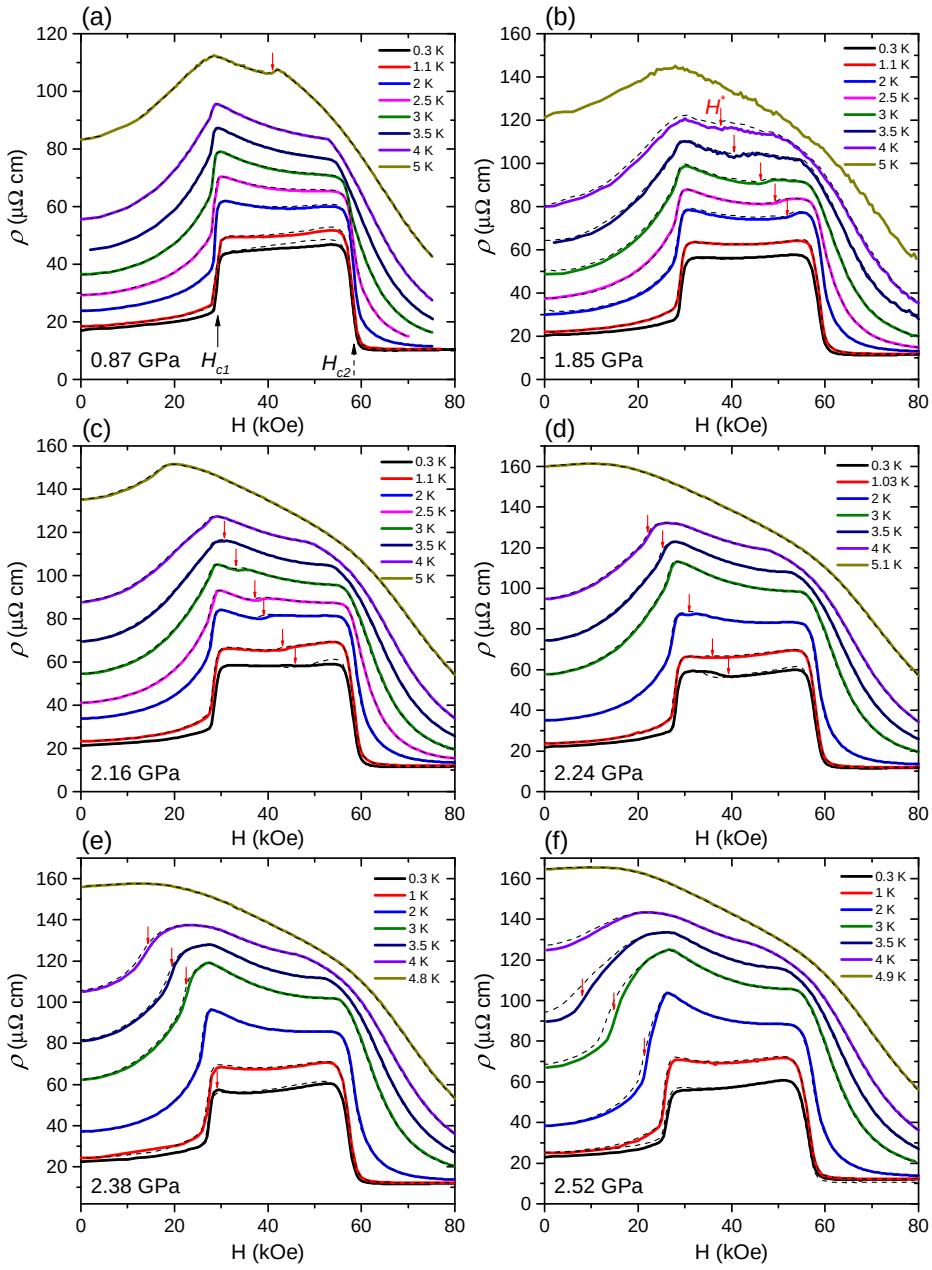

Figure S4. In-plane magnetoresistance of $CeAuSb_2$ at various applied pressures and temperatures below T_N. Magnetic fields are applied along the c-axis. Solid lines represent upsweeps and dashed lines represent downsweeps. The arrows indicate the critical fields H_{c1}, H_{c2} and H^*.

Figure S5 shows the derivative of the in-plane magnetoresistance, $\mathrm{d}\rho/\mathrm{d}H$, at various applied pressures and temperatures. As shown in Fig. S5(a),(d),(g), and (j), at low temperature a sharp peak marked by blue arrows in $\mathrm{d}\rho/\mathrm{d}H$ occurs at H_{c1} for all pressures. The amplitude of the peak is reduced with increasing temperature; however, the peak position just moves slightly with increasing temperature. Figures S5(b),(e),(h), and (k) show the field dependence of $\mathrm{d}\rho/\mathrm{d}H$ near H^*. At low pressure, H^* marked by red arrows in $\mathrm{d}\rho/\mathrm{d}H$ appears between H_{c1} and H_{c2} and decreases with increasing temperature. Above 2.16 GPa, however, H^* moves to lower fields upon crossing H_{c1}, inducing a merging of two peaks from the first MM transition and a new transition. Therefore, in this broad peak a subsidiary shoulder occurs at H_{c1} at high pressure as shown in Fig. S5(k). Figures S5(c),(f),(i) and (l) show the field dependence of $\mathrm{d}\rho/\mathrm{d}H$ near H_{c2}. At 0.87 GPa, a sharp peak at H_{c2} indicated by black arrows does not move up to 3 K. Above 3.5 K, however, this peak becomes broader and H_{c2} decreases with increasing temperature suggesting that a tricritical point of H_{c2} is located between 3 and 3.5 K at 0.87 GPa. A previous report, Ref. 19 of main text, already observed the tricritical point of H_{c2} near 3.7 K at ambient pressure. In our results, the tricritical point is observed near 3 K at 2.16 GPa as shown in Fig. S5(f). Therefore, the tricritical point decreases to 3 K with increasing pressure to 2.16 GPa. However, T_N in zero applied field also decreases from 6.8 K to 5 K with pressure up to 2.16 GPa. Above 2.16 GPa, the tricritical point of H_{c2} does not change with pressure.

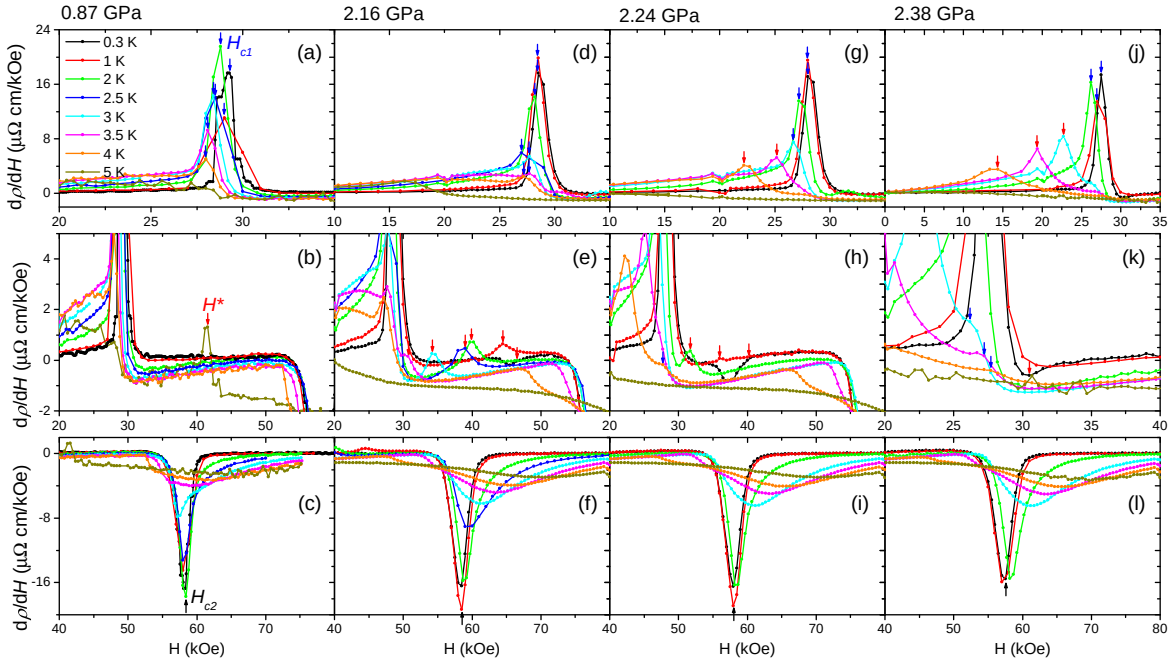

Figure S5. Pressure and temperature dependence of the magnetic field derivative of the magnetoresistance of $CeAuSb_2$.

IV. PHASE DIAGRAMS OF $CeAuSb_2$

Figures S6 displays the temperature dependence of the resistivity derivative at various magnetic fields applied along the c-axis. Up to 2.24 GPa, at zero field a sharp peak including coupled magnetic-structural transitions occurs at $T_N + T_{\mathrm{nem}}$ marked by black arrow as shown in Fig. S6(a) and (b). Under applied magnetic field, this coupled transition turns into two transitions, an antiferromagnetic(AFM) phase transition at T_{N2} and a new phase transition at T^*, indicated by blue arrows and orange arrows, respectively. Both T_{N2} and T^* are suppressed with field. The splitting field decreases with increasing pressure, and finally at 2.38 GPa, two separate peaks in $\mathrm{d}\rho/\mathrm{d}T$ occur at $T_{\mathrm{nem}} = T_N$ and T_{N2} at zero field as shown in Fig S6(c). In the main text, from the $T - P$ phase diagram in zero applied field we propose that a simultaneous first-order structural and magnetic phase transition occurs at $T_{\mathrm{nem}} = T_N$ marked by red arrow. $T_{\mathrm{nem}} = T_N$ is suppressed below 2 K near H_{c1}.

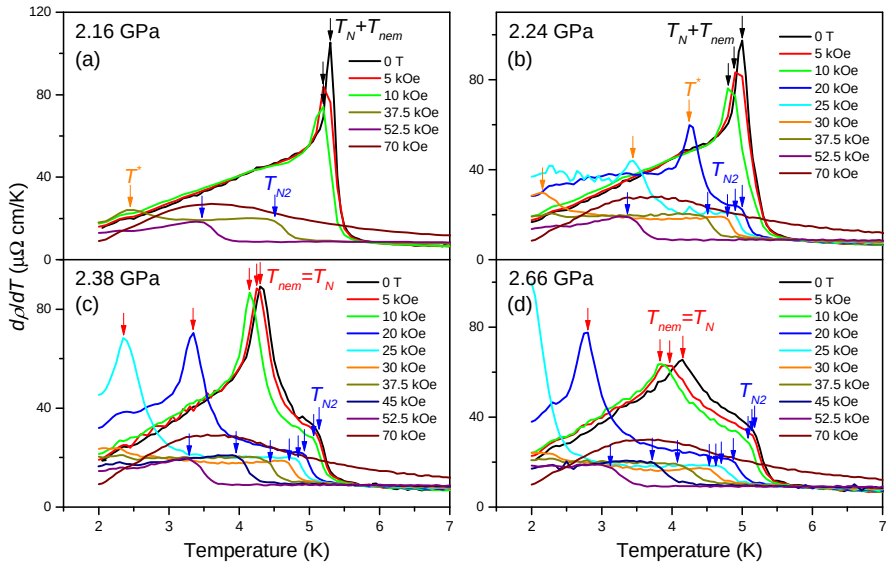

Figure S6. Temperature dependence of the in-plane resistivity derivative at various magnetic fields applied along the c-axis. Arrows indicate the distinct phase transitions.

Figures S7 shows the $H-T$ phase diagram constructed based on the data displayed in Figs. S4-S6. Solid symbols indicate critical magnetic fields from magnetoresistance and open symbols indicate phase transition temperatures from temperature dependence of resistivity. The AFM phase transitions, $T_N+T_{\rm nem}$ at low pressure and T_{N2} at high pressure, are connected to H_{c2}. The field dependence of AFM transition temperatures, and temperature dependence of H_{c1} and H_{c2} do not change much with pressure. The new first-order phase transition H^* is matched with T^* above H_{c1} and with $T_{\rm nem}=T_N$ below H_{c1}. Above 1.51 GPa, new phases appear in multi-q region in AFM phase diagram for $CeAuSb_2$ as shown in Fig. S7(c). The new phase transition line indicated by blue symbols gradually decreases to lower fields with increasing pressure inducing new phases (M', M", and M*). Above 2.24 GPa, the coupled transition turns into two transitions at T_{N2} and $T_{\rm nem}=T_N$ at zero field. Figure S7(f),(g), and (h) exhibit that the field dependence of a second-order AFM transition at T_{N2} and a simultaneous first-order structural and magnetic phase transition at $T_{\rm nem}=T_N$ at high pressure.

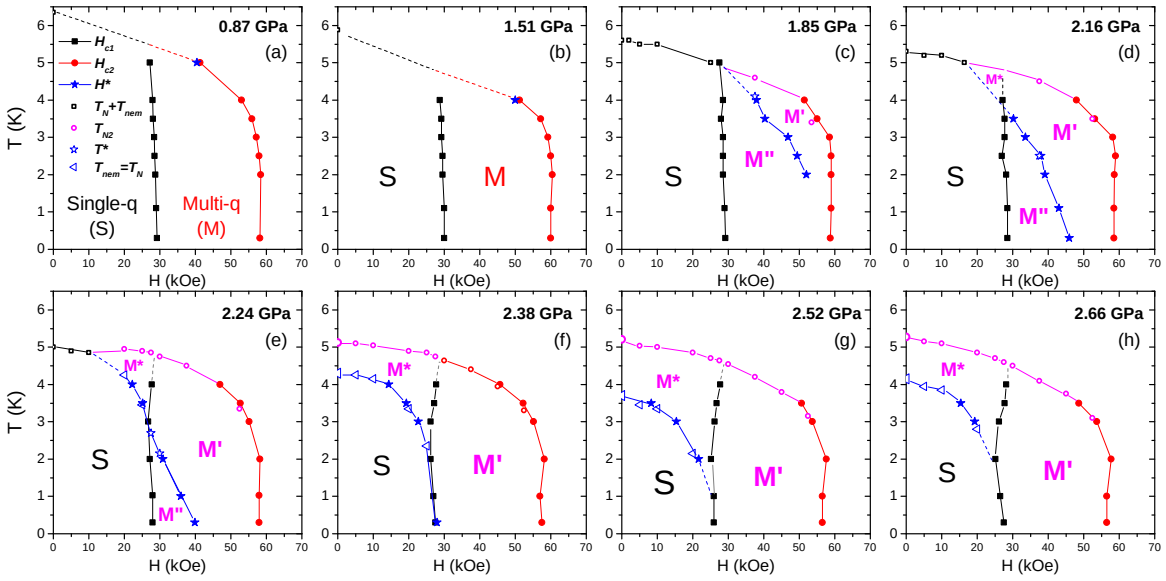

Figure S7. $H-T$ phase diagram of $CeAuSb_2$ at various applied pressures.